JACS
JOURNAL OF THE AMERICAN CHEMICAL SOCIETY
Article
pubs.acs.org/JACS

Molecular Beam Epitaxy of Highly Crystalline Monolayer Molybdenum Disulfide on Hexagonal Boron Nitride

Deyi Fu,[†,‡,○] Xiaoxu Zhao,[‡,○] Yu-Yang Zhang,[§,¶] Linjun Li,[∥] Hai Xu,[‡] A-Rang Jang,[⊥] Seong In Yoon,[⊥] Peng Song,[‡] Sock Mui Poh,[‡] Tianhua Ren,[‡] Zijing Ding,[∥] Wei Fu,[‡] Tae Joo Shin,[#] Hyeon Suk Shin,[⊥] Sokrates T. Pantelides,[¶] Wu Zhou,[§,▽] and Kian Ping Loh*[,†,‡,∥]

[†]SinBeRISE CREATE, National Research Foundation, CREATE Tower, 1 Create Way, Singapore 138602, Singapore

[‡]Department of Chemistry, National University of Singapore, 3 Science Drive 3, Singapore 117543, Singapore

[§]School of Physical Sciences, CAS Key Laboratory of Vacuum Physics, University of Chinese Academy of Sciences, Beijing 100049, China

[∥]Centre for Advanced 2D Materials and Graphene Research Centre, National University of Singapore, 6 Science Drive 2, Singapore 117546, Singapore

[⊥]Department of Chemistry, Department of Energy Engineering, Low Dimensional Carbon Materials Center, and [#]UNIST Central Research Facilities, UNIST (Ulsan National Institute of Science and Technology), Ulsan 44919, Republic of Korea

[▽]Materials Science and Technology Division, Oak Ridge National Laboratory, Oak Ridge, Tennessee 37831, United States

[¶]Department of Physics and Astronomy and Department of Electrical Engineering and Computer Science, Vanderbilt University, Nashville, Tennessee 37235, United States

Supporting Information

ABSTRACT: Atomically thin molybdenum disulfide (MoS_2), a direct-band-gap semiconductor, is promising for applications in electronics and optoelectronics, but the scalable synthesis of highly crystalline film remains challenging. Here we report the successful epitaxial growth of a continuous, uniform, highly crystalline monolayer MoS_2 film on hexagonal boron nitride (h-BN) by molecular beam epitaxy. Atomic force microscopy and electron microscopy studies reveal that MoS_2 grown on h-BN primarily consists of two types of nucleation grains (0° aligned and 60° antialigned domains). By adopting a high growth temperature and ultralow precursor flux, the formation of 60° antialigned grains is largely suppressed. The resulting perfectly aligned grains merge seamlessly into a highly crystalline film. Large-scale monolayer MoS_2 film can be grown on a 2 in. h-BN/sapphire wafer, for which surface morphology and Raman mapping confirm good spatial uniformity. Our study represents a significant step in the scalable synthesis of highly crystalline MoS_2 films on atomically flat surfaces and paves the way to large-scale applications.

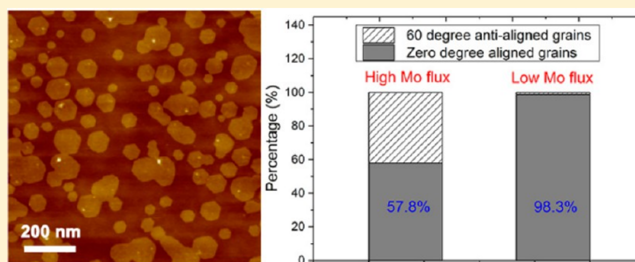

■ INTRODUCTION

As one of the most stable semiconducting transition metal dichalcogenides (TMDCs), molybdenum disulfide (MoS_2) has been extensively studied for its interesting optoelectronic properties.[1−8] Atomically thin crystals of MoS_2 can be obtained by using techniques such as mechanical exfoliation,[9] chemical intercalation,[10] and chemical vapor deposition (CVD).[11,12] Among these techniques, CVD has emerged as the most promising technique for the growth of large monolayer crystals on various substrates. By tuning the growth conditions, isolated single crystalline monolayer MoS_2 flakes with sizes up to several hundred micrometers have been successfully grown.[13,14] Despite these achievements, a major drawback in vapor transport methods is the insufficient control of the uniformity of the film, which leads to the formation of mosaic-like polycrystalline films. The growth of monolayer MoS_2 films with wafer-scale uniformity by metal−organic chemical vapor deposition has been reported recently.[15] However, as is typically observed in nonepitaxial growth, the film was polycrystalline with a high density of grain boundaries[16,17] arising from the coalescence of randomly oriented nucleation domains. There are also efforts to grow a large-area MoS_2 film on epitaxial substrates such as mica and sapphire.[18,19] Although the number of misaligned domains has been largely reduced due to the epitaxial growth mechanism, the films still contain a high density of grain boundaries. Grain boundaries are known to be deleterious to both the electrical and mechanical performance of 2D films; for example, the tilt grain boundary in MoS_2 can dramatically degrade its mobility.[20] Moreover, the

Received: May 22, 2017
Published: June 21, 2017

ACS Publications © 2017 American Chemical Society

DOI: 10.1021/jacs.7b05131
J. Am. Chem. Soc. 2017, 139, 9392−9400

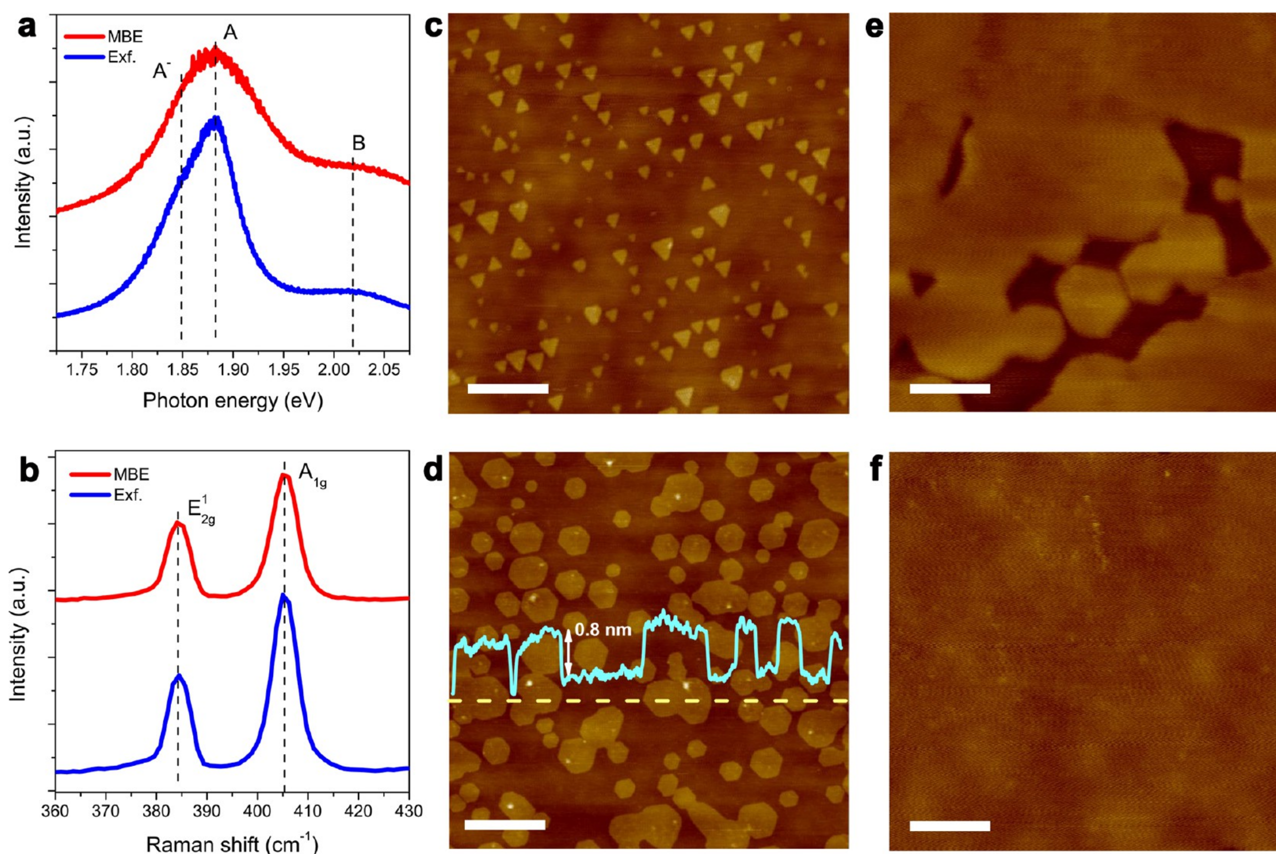

Figure 1. Epitaxial growth of monolayer MoS_2 film. (a) Photoluminescence and (b) Raman spectra of an as-grown monolayer MoS_2 film on h-BN (red curves) under 532 nm confocal laser excitation. Corresponding results for exfoliated single crystalline MoS_2 monolayers on h-BN are also shown for comparison (blue curves). The Raman spectra are vertically offset for better illustration. (c−f) AFM scans at different growth stages: (c) nucleation of isolated seed grains (triangles), (d) enlarged grains with hexagonal shape (transformed from triangular grains), (e) partially coalesced film from hexagonal grains, (f) seamless, uniform monolayer film. The height profile along the dashed line in d confirms the monolayer thickness (~0.8 nm) of MoS_2. Scale bars: (c−f) 200 nm.

ubiquitous presence of dangling bonds and charge traps on conventional oxide substrates means that the excellent potential of these films cannot be fully exploited. Therefore, the scalable epitaxial growth of highly crystalline films on surfaces that are free from dangling bonds is highly desired.

Currently, the ability to control domain orientation and suppress grain boundary formation remains a challenge in the growth of TMDCs. This problem is compounded by the relatively low energy barrier for the generation of rotational disorder and dislocations in TMDCs. Previous reports on the CVD growth of MoS_2 on hexagonal boron nitride (h-BN) largely showed randomly oriented MoS_2 domains.[21−24] To investigate the nucleation and fusion of isolated grains, methods need to be developed to grow samples where the density, geometrical orientation, and morphology of grains can be precisely controlled. Here we report the successful epitaxial growth of a continuous, uniform, highly crystalline monolayer MoS_2 film on h-BN by molecular beam epitaxy (MBE).[25−27] We develop a two-step nucleation and growth process in MBE, where regularly shaped domains with only two types of orientations (0° and rotated by 60°) are initially formed. During the subsequent growth step, all the domains merge seamlessly to form continuous films. Recently, Hua Yu et al. have reported controlled growth of MoS_2 on h-BN by CVD,[28] where two grain orientations (0° and 60°) with equal proportions are present. In our MBE-grown film, however, we have markedly suppressed 60° antialigned grain formation, leading to a highly crystalline film with negligible grain boundaries. As a proof-of-concept, we have grown a uniform monolayer MoS_2 film on a 2 in. h-BN/sapphire wafer. Our growth method is also applicable to other TMDCs and paves the way to achieving the controllable and scalable synthesis of highly crystalline TMDC films on atomically flat surfaces.

■ RESULTS AND DISCUSSION

Epitaxial Growth of Monolayer MoS_2 Film. In preliminary growth experiment, single-crystalline h-BN flakes exfoliated from high-quality bulk crystals were used as epitaxial growth templates, and a 285-nm-thick SiO_2/Si wafer served as the supporting substrate. The growth was carried out in the temperature range 750−900 °C in a dedicated MBE setup (see Experimental Section). Ultrapure molybdenum (Mo) and sulfur (S) molecular beams were evaporated by an e-beam evaporator and a valved sulfur cracker cell, respectively, to serve as reaction precursors. In order to suppress vertical nucleation (island growth, Figure S1) and promote growth by edge attachment (lateral growth), a two-step growth strategy was adopted: In the first step, the substrate temperature was adjusted to ~750 °C and Mo and S molecular beams were introduced onto the heated substrate surface to react for 3 to 4 h, allowing the formation of isolated nuclei on h-BN (Figure 1c). In the second step, the substrate temperature was increased to ~900 °C, during which the Mo flux was decreased. The precursor flux ratio was adjusted so that the initial triangular

DOI: 10.1021/jacs.7b05131
J. Am. Chem. Soc. 2017, 139, 9392−9400

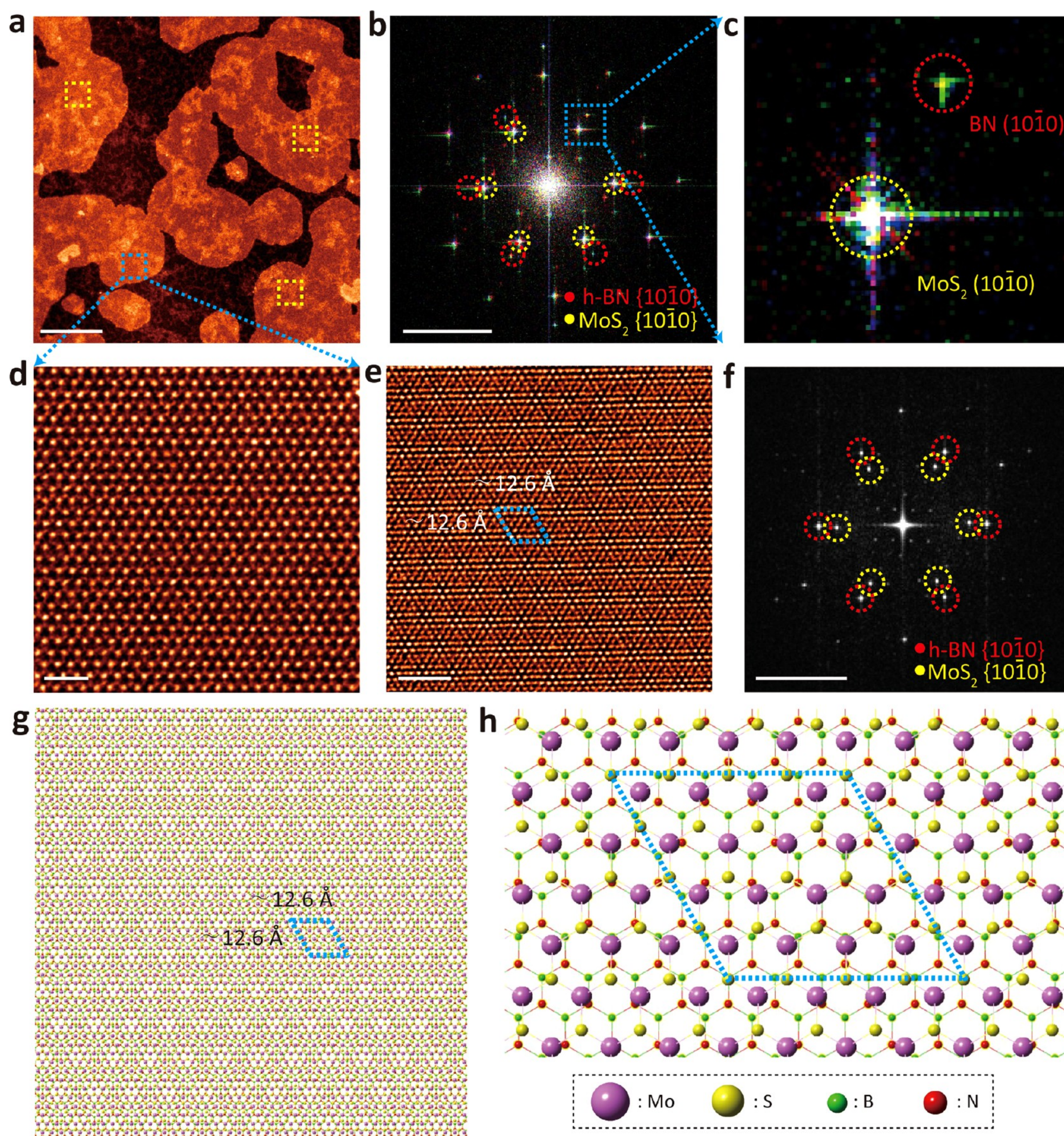

Figure 2. Epitaxial growth mode and structure of monolayer MoS_2 on h-BN. (a) STEM-ADF image of a typical sample with ~70% MoS_2 coverage on h-BN. (b) Overlaid FFT patterns of the three yellow box regions showing identical orientations and (c) enlarged region showing characteristic (10$\bar{1}$0) spots of MoS_2 and h-BN. (d) Atom-resolved STEM-ADF image of a typical high-quality MoS_2 monolayer film. (e) STEM-BF image of a MoS_2/h-BN vdW heterostructure showing a periodic moiré pattern and (f) the corresponding FFT pattern. (g) Atomic model of the moiré pattern in e and (h) the zoom-in atomic arrangement. Scale bars: (a) 100 nm; (b, f) 5 nm^{-1}; (d) 1 nm; (e) 2 nm.

nucleation domains gradually transformed into well-aligned hexagonal crystals (Figure 1d). The growth process continued for 6 to 7 h to form a completely seamless film covering the whole h-BN substrate.

The as-grown MoS_2 film was first characterized by photoluminescence (PL) and Raman scattering spectroscopy, as shown in Figure 1a,b. The spectra from mechanically exfoliated single crystalline MoS_2 monolayers on h-BN flakes are plotted also for comparison. As indicated by the dashed lines in Figure 1a, the main peak located at ~1.88 eV is attributed to A-excitonic emission of MoS_2,[29] while the two shoulder peaks correspond to trion (A^-) and B-excitonic emissions, respectively.[21] The relative intensity between trion (A^-) and A-excitonic emissions in the two cases are slightly different, which may originate from the different strengths of interlayer coupling of the MoS_2 monolayers with h-BN. The two Raman peaks located at ~384.4 and ~405.4 cm^{-1} correspond to the in-plane E_{2g}^{1} mode and the out-of-plane A_{1g} mode of monolayer MoS_2,[30] respectively, yielding a peak separation of ~21.0 cm^{-1} for both as-grown and exfoliated

DOI: 10.1021/jacs.7b05131
J. Am. Chem. Soc. 2017, 139, 9392−9400

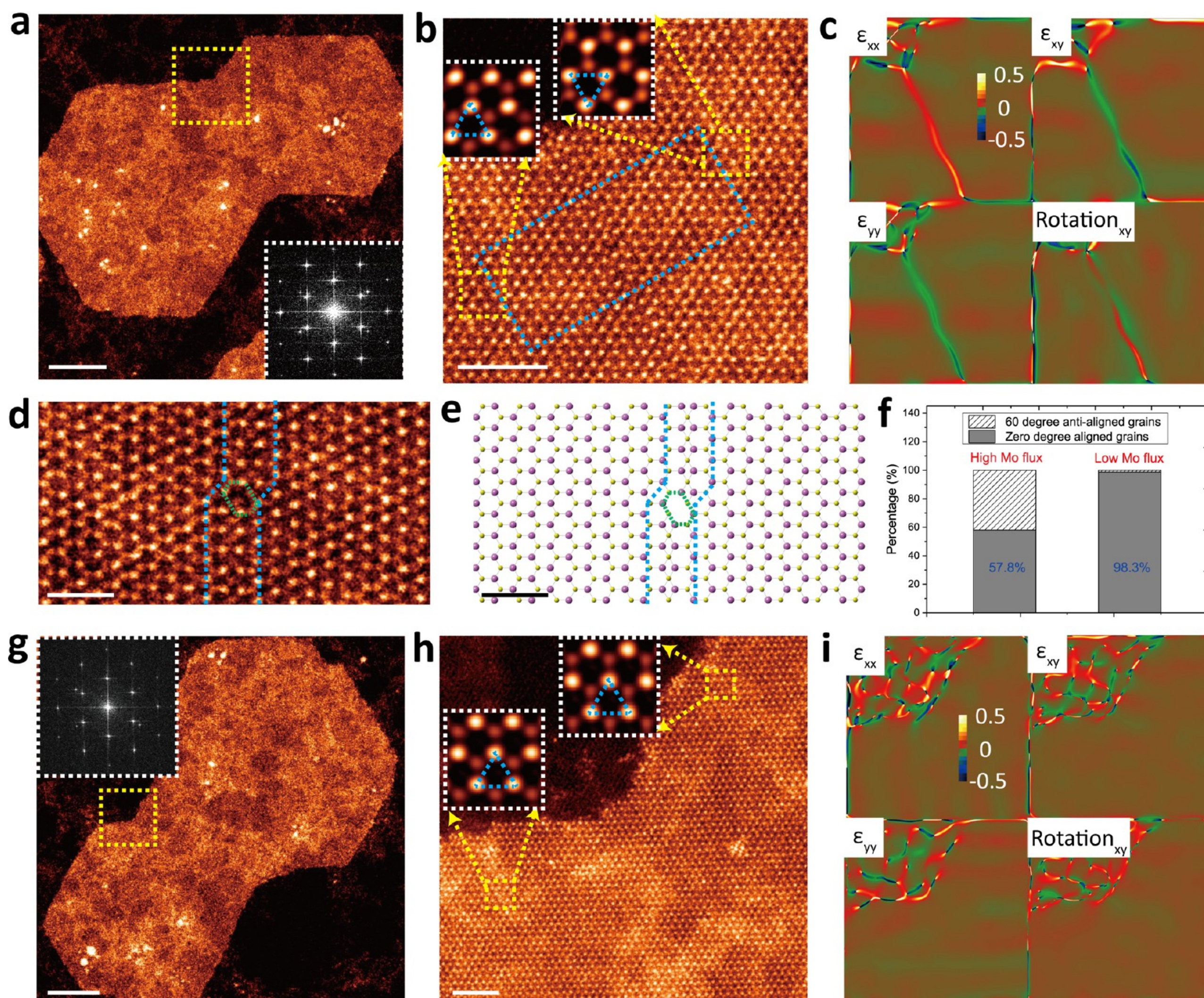

Figure 3. Merging behavior of adjacent MoS_2 grains. (a) STEM-ADF image of two merged grains with 60° misorientation and (b) the magnified view of the merging area indicated by the yellow box in a. The Mo triangles highlighted by the blue dashed lines indicate that the two grains have 60° rotational mismatch. (c) Strain field mapping of the whole area shown in b using the matrix series ε_{xx}, ε_{xy}, ε_{yy} and rotation$_{xy}$. (d) Enlarged GB area of the blue box in b showing an S-4|4P type 60° m-GB with an 8-fold ring highlighted in green and (e) its corresponding atomic model. (f) Histogram of the percentage of MoS_2 grains with various orientations under different Mo flux. (g) STEM-ADF image of two merged grains with 0° misorientation and (h) the magnified view of the merging area indicated by the yellow box in g. The Mo triangles highlighted by the blue dashed lines indicate that the two grains have the same orientation. (i) Strain field mapping of the whole area shown in h using ε_{xx}, ε_{xy}, ε_{yy} and rotation$_{xy}$. Scale bars: (a, g) 20 nm; (b, h) 2 nm; (d, e) 1 nm.

samples. These consistent values further confirm the monolayer thickness of our film as well as similar interlayer coupling with the h-BN substrate in both cases. More importantly, we found that the full-width-at-half-maximum (FWHM) of the E_{2g}^{1} peak in our film is comparable to that in other as-prepared single-crystalline MoS_2 monolayers (Figure S2), pointing to the excellent crystalline quality of the film. The high uniformity and continuity of the as-grown film can be seen from the PL and Raman mapping shown in Figure S3.

The morphological evolution of the nucleated crystals was studied using atomic force microscopy (AFM), as shown in Figure 1c–f. During the first growth step, the majority of the MoS_2 seeds are aligned with the h-BN substrate along one direction, which we call 0° aligned grains, and a minority of the grains are rotated 60° from this main alignment direction, which we henceforth call 60° antialigned grains. It was found that Mo flux showed a strong influence on the orientations of the nuclei (Figure S4), and an ultralow Mo flux is needed to allow the growth to be thermodynamically equilibrated; that is, grains tend to align in one direction. By tuning the growth temperature and precursor flux ratio in the second growth step, these triangular grains gradually transformed into hexagonal-shaped grains (Figure 1d). With increasing growth time, these nuclei gradually enlarged and merged with each other (Figure 1e). Finally, all the grains coalesced seamlessly, forming a continuous film covering the entire h-BN surface uniformly (Figure 1f and Figure S5). The cross-sectional height profile shown in Figure 1d confirmed the monolayer thickness of the as-grown film. The growth adopts a layer-by-layer growth mode; that is, the second layer nucleation did not start until the completion of the first layer.

Structural Characterization of Monolayer MoS_2. Next, atomic resolution scanning transmission electron microscopy (STEM) was employed to characterize the crystallinity of the as-grown MoS_2 film. A typical sample with ~70% monolayer coverage was studied, as shown in Figure 2a. To confirm

DOI: 10.1021/jacs.7b05131
J. Am. Chem. Soc. 2017, 139, 9392−9400

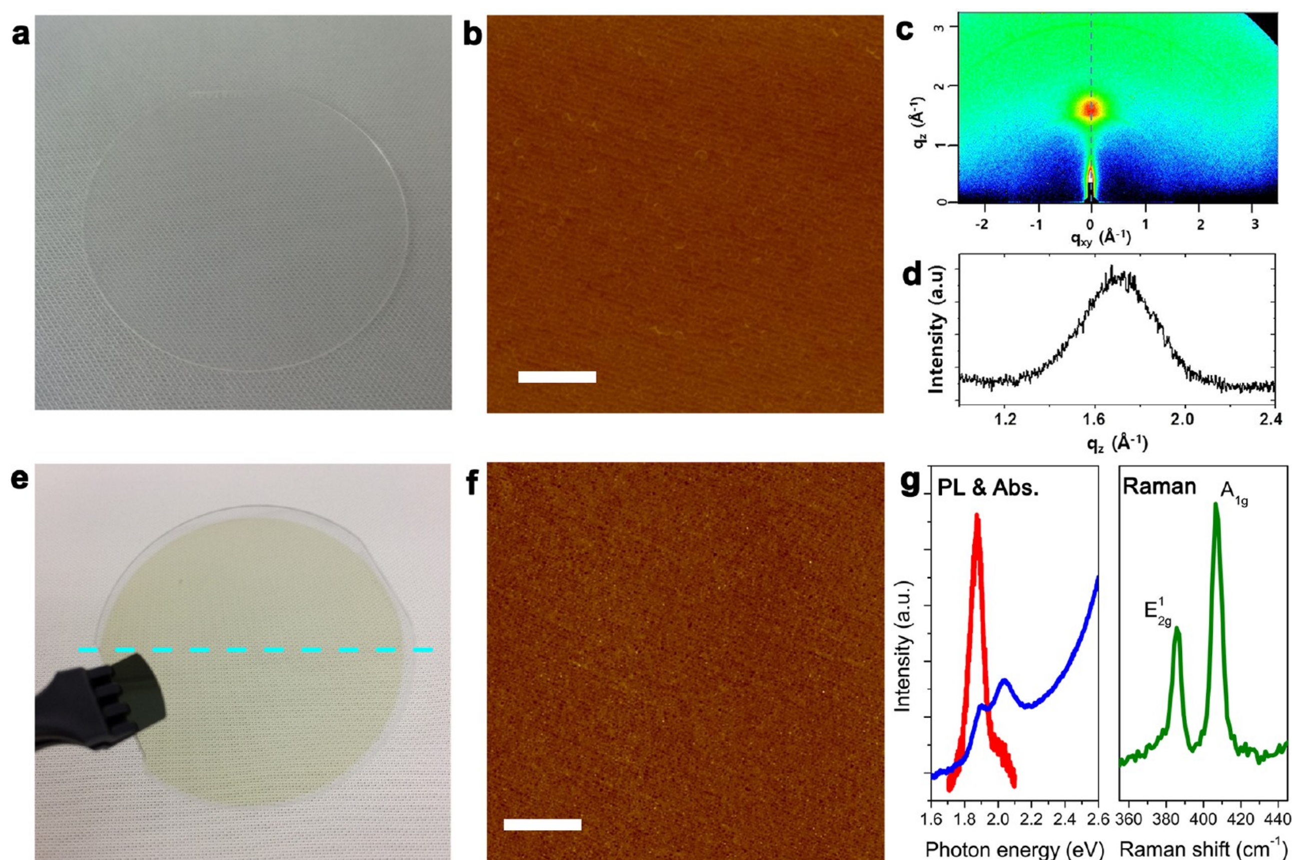

Figure 4. Growth of a wafer-scale monolayer MoS_2 film. (a) Photograph of a 2 in. h-BN wafer grown on a sapphire substrate. (b) AFM scan of the multilayer h-BN surface. RMS roughness is 0.155 nm. (c) Grazing incidence wide-angle X-ray diffraction (GI-WAXD) mapping of the h-BN film. (d) Out-of-plane GI-WAXD q_z profile along the dashed line in c. According to Bragg's law, $d = 2\pi/q_z$, the (0002) d-spacing in h-BN is determined to be 3.791 Å. (e) Photograph of the as-grown monolayer MoS_2 film on a 2 in. h-BN/sapphire wafer. (f) AFM scan of the MoS_2 film surface. RMS roughness is 0.206 nm. (g) Photoluminescence (PL, red), absorption (Abs., blue), and Raman (green) spectra measured at a random location of the monolayer MoS_2 film. Note that the characteristic PL and Raman signals from the h-BN/sapphire substrate have been subtracted (Figure S11). Scale bars: (b, f) 1 μm.

epitaxial growth and homogeneity, we performed high-resolution STEM imaging of three randomly chosen regions, as indicated by the yellow boxes, and the corresponding fast Fourier transform (FFT) patterns are overlaid in Figure 2b. The characteristic $(10\bar{1}0)$ spots of MoS_2 and h-BN are depicted in Figure 2c. As can be seen, the MoS_2 diffraction spots follow the crystallographic orientation of the underlying h-BN substrate, and all three sets of spots superposed on each other exactly. Atom-resolved STEM-annular dark field (STEM-ADF) imaging from several random regions shown in Figure S6 reveals that they are all oriented in the same direction. Statistical sampling at more locations further confirms the uniform orientation of the as-grown film. Therefore, it can be concluded that MoS_2 grows epitaxially on h-BN to form a near single-crystalline film.

Figure 2d depicts a typical STEM-ADF image of the MoS_2 film on a thin h-BN flake, where a perfect MoS_2 lattice without any extended structural defects is observed. Since the contrast in ADF imaging depends on atomic number (Z), the h-BN substrate composed of light elements is not visible in the ADF image. In order to visualize the long-range moiré superlattice formed in the MoS_2/h-BN van der Waals (vdW) heterostructure, STEM bright-field (BF) phase contrast imaging was applied. As depicted in Figure 2e, a well-defined moiré pattern is observed in the MoS_2/h-BN vdW heterostructure with a periodicity of ~12.6 Å, which is further confirmed by the presence of additional superstructure spots with large d-spacing in the corresponding FFT pattern (Figure 2f). Monolayer MoS_2 and h-BN have a lattice constant of ~3.16 Å[31] and ~2.51 Å,[32] respectively. The moiré pattern thus corresponds to a superlattice of 4 × 4 MoS_2 unit cells and 5 × 5 h-BN unit cells and exhibits the same crystallographic orientation as both component layers. This can be better explained from the atomic model of the MoS_2/h-BN vertical heterostructure with epitaxial alignment shown in Figure 2g,h. It is clearly seen that the superimposition of the atoms in the two layers reproduces the moiré pattern obtained in the experimental image quite well (Figure 2e). To determine the detailed stacking registry between MoS_2 and h-BN from the experimental images, however, is still challenging. Some of the possible registries are listed in Figure S7.

Merging Behavior of MoS_2 Grains. The coalescence of MoS_2 grains on the h-BN surface was further investigated by STEM-ADF imaging. Figure 3a is a STEM-ADF image showing the merging behavior of two grains rotated by 60° in a test sample. The merging area is indicated by the yellow box, and its corresponding FFT pattern is shown in the inset, where a single set of spots in a hexagonal pattern is observed. The 60° rotational mismatch between the two merging MoS_2 grains can be clearly identified from the atom-resolved STEM-ADF image

DOI: 10.1021/jacs.7b05131
J. Am. Chem. Soc. 2017, 139, 9392−9400

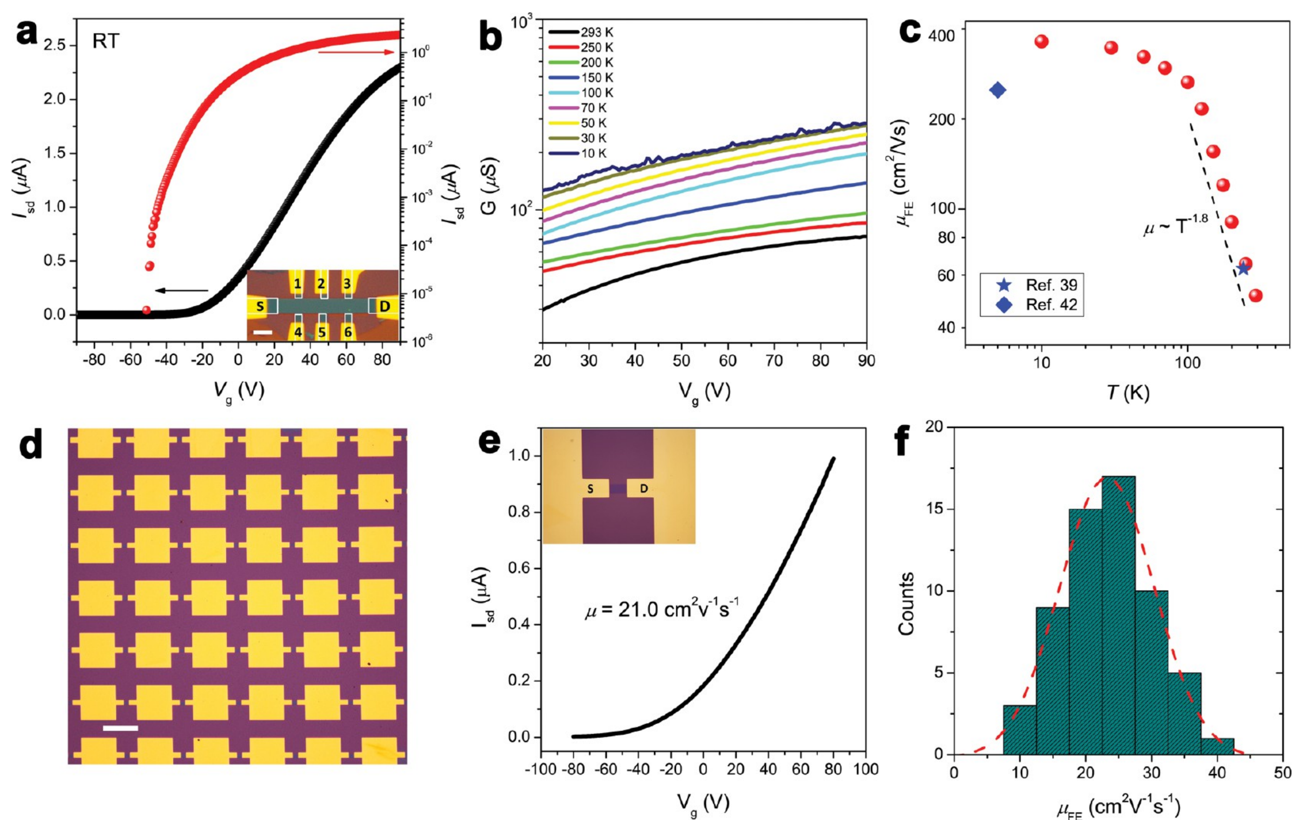

Figure 5. Transport properties of monolayer MoS_2 FETs made from film grown on exfoliated h-BN (a−c) and wafer-scale h-BN (d−f). (a) Two-probe transfer curve of a back-gated MoS_2 FET measured at room temperature. The source−drain bias was fixed at 0.5 V. Inset: Photograph of the multiterminal FET device made from a monolayer MoS_2 film grown on exfoliated h-BN. The channel is capped by an h-BN thin flake, and the electrodes are contacted by graphene, as outlined by the white boxes. (b) Four-probe transfer curves of the FET in panel a taken at different temperatures. Voltage was recorded between probe leads 1 and 2. (c) Temperature dependence of the field-effect mobility μ_{FE} extracted from panel b. At temperatures above ~100 K, μ_{FE} is limited by phonon scattering, which can be fitted by a power law $T^{-\gamma}$. (d) Optical image of a FET device array fabricated from a wafer-scale monolayer MoS_2 film grown on h-BN/sapphire. The MoS_2/h-BN film was first transferred onto a 285 nm SiO_2/Si substrate before device fabrication. (e) Two-probe transfer curve of a typical FET in part d measured at room temperature. The source−drain bias was fixed at 0.1 V. Inset: Photograph of the FET device with a channel length of 20 μm and width of 10 μm. (f) Histogram of field-effect mobility measured on 60 devices in panel d. Scale bars: (a) 5 μm, (d) 100 μm.

by looking at the orientation of Mo triangles in the hexagonal ring (inset of Figure 3b). Specifically, the arrangement of Mo atoms in the two grains is mirror symmetric, therefore forming a mirror grain boundary (m-GB) as indicated in the blue box. The detailed atomic structure of the m-GB is further revealed in Figure 3d. Theoretical studies[33] have shown that up to eight types of m-GBs can potentially exist. However, only two types are observed here. Specifically, the dominant m-GB shown in Figure 3d with the corresponding atomic model in Figure 3e comprises a row of 4-fold rings having an S_2 point sharing site, referred to as S-4|4P m-GB. The other type, S-4|4E m-GB, is composed of a string of 4-fold rings having a Mo−S edge, which is only occasionally observed, and is depicted in Figure S8. These two types of m-GBs have been predicted[34] and experimentally proven to be perfect metallic quantum wires.[35] Geometric phase analysis (GPA)[36] was further applied to analyze the level of strain associated with the GBs. Mappings of a symmetric strain matrix series (ε_{xx}, ε_{xy}, ε_{yy} and rotation$_{xy}$) are presented in Figure 3c. Notably, the strain is concentrated only along the GB, while the rest of the film is both strain-free and dislocation-free.

A typical STEM-ADF image of two merged MoS_2 grains with no rotational mismatch is illustrated in Figure 3g. The magnified image confirms that the two grains have exactly the same orientation, and no m-GBs were observed in the whole merging area (Figure 3h). To further validate this perfect merging behavior, routine GPA was used to inspect the possible presence of associated strain or dislocation. The strain maps shown in Figure 3i clearly indicate a homogeneous MoS_2/h-BN heterostructure without any imperfections.

As mentioned before, it is possible to achieve high alignment of grains at the early nucleation stage by growing at a high temperature and using an ultralow Mo flux. In order to verify that the density of 60° antialigned grains can be reduced by decreasing the Mo flux at high growth temperature so as to facilitate a thermodynamically equilibrated process, we have grown two control samples at the same temperature (750 °C) with distinctly different Mo flux. A statistical analysis of the crystal orientations of nucleated grains across a total area of ~10 μm² is shown in Figure 3f. As can be seen, by lowering Mo flux, the proportion of 60° antialigned grains decreases drastically from about ~42% to ~1.3%, which means that most of the grains are aligned in the same direction. As discussed above, the grains with the same orientation will merge perfectly without forming any grain boundary. Therefore, we conclude that a near single crystalline monolayer MoS_2 film has been successfully synthesized by our two-step growth method.

DOI: 10.1021/jacs.7b05131
J. Am. Chem. Soc. 2017, 139, 9392−9400

Growth of Wafer-Scale Monolayer MoS_2 Film. In order to examine the scalability of our epitaxial growth, a large h-BN template prepared by CVD on a 2 in. sapphire wafer (Figure 4a) was used.[37] The h-BN film was grown at high temperature to ensure good crystallinity, and its typical thickness is 2−6 layers. Successful growth of a multilayer h-BN film was confirmed by X-ray photoelectron spectroscopy (XPS) and UV/vis absorption spectroscopy (Figure S9). The highly smooth and uniform h-BN film was further characterized by AFM scanning and grazing-incidence wide-angle X-ray diffraction (GI-WAXD) mapping. The AFM image in Figure 4b exhibits a very smooth surface without any wrinkles. The root-mean-square roughness (R_z) is 0.155 nm, which is very similar to that of the annealed bare sapphire (R_z = 0.102 nm). Figure 4c,d show the GI-WAXD mapping and q_z profile of the h-BN film. The interlayer distance of the h-BN film measured by GI-WAXD is ∼3.67 Å, which is slightly larger than that in bulk h-BN (∼0.33 nm) possibly due to corrugation originating from the interaction with the sapphire substrate. These characterization results verify that the h-BN film is an ideal template for wafer-scale MoS_2 growth.

The as-grown monolayer MoS_2 film shown in Figure 4e (yellowish area) can be easily distinguished from the transparent h-BN/sapphire substrate at the borders. The PL, absorption, and Raman spectra show typical characteristics of high-quality MoS_2 monolayers (Figure 4g). The PL peak position (∼1.88 eV) and Raman peak separation (∼21.0 cm^{-1}) are identical to those of monolayer films grown on exfoliated h-BN flakes. It should be noted that the FWHM of the MoS_2 characteristic Raman peak E_{2g}^{1} is slightly larger than that of the MoS_2 grown on exfoliated h-BN (Figure S2), indicating a lower crystal quality of the wafer-scale film. The growth quality of the epilayer is mainly limited by the polycrystalline nature of the 2-in. h-BN film that will cause misorientation of MoS_2 domains. We further performed AFM scanning and spectral mapping of the Raman peaks at randomly selected regions along the dashed line in Figure 4e. The surface morphology and contour plot of the Raman peak separation are shown in Figure 4f and Figure S10, respectively. The smooth surface and uniform distribution of the peak separation confirm the homogeneity of the whole film. Since the growth of large-area h-BN films has already been proven to be viable,[37,38] a major bottleneck in the van der Waals epitaxy of 2D TMDCs is thus removed, enabling the realization of large-area TMDC/h-BN vertical hybrids.

Device Performance of Monolayer MoS_2. The transport property of the MBE-grown MoS_2 films on exfoliated h-BN was evaluated by fabricating field-effect transistors (FETs). To reduce adverse effects due to contact resistance, we fabricated a MoS_2 FET with multiterminal configuration[39,40] (inset of Figure 5a). First, a pre-etched multilayer graphene was transferred onto the as-grown MoS_2 film to afford gate-tunable contact electrodes.[41] Next, the graphene/MoS_2/h-BN stack was etched into a Hall bar structure using a deep reactive ion etcher following which Ti/Au was deposited on top of the contact leads to form graphene−metal contacts. Finally, an h-BN flake (∼20 nm thick) was capped onto the channel area to form the h-BN/MoS_2/h-BN sandwich structure. By encapsulating MoS_2 with the atomically flat h-BN, impurity scattering can be more effectively suppressed due to the more efficient screening of charged impurities.

A typical two-probe transfer curve is shown in Figure 5a in both linear and log scales. The increase of source−drain current with positive gate bias confirms the N-type conduction in our film, as reported for all as-synthesized MoS_2 crystals. For a source−drain bias voltage of 0.5 V, the device exhibits an ON/OFF ratio of $\sim 10^6$ and a maximal ON-current of ∼2.3 μA. In order to further eliminate contact effects, we measured the device in a four-probe configuration, where a source−drain current of 100 nA was applied while the voltage drop between adjacent voltage probe leads (1 and 2) was recorded. The four-probe transconductance is defined by $G = I_{sd}/|V_1 - V_2|$. Figure 5b shows the detailed transfer characteristics at different temperatures. It is seen that with decreasing temperature G increases monotonically over the entire V_g range. This metallic behavior is observed in all our graphene-contacted devices and has also been reported by other groups;[39,40] this observation further confirms the negligible contact resistance in our devices. The temperature-dependent mobility of the device is extracted from Figure 5b and shown in Figure 5c. At room temperature, the mobility is ∼45 $cm^2\ V^{-1}\ s^{-1}$ and increases to ∼375 $cm^2\ V^{-1}\ s^{-1}$ when the temperature is decreased to 20 K. All these results are comparable to the best values (symbols in Figure 5c) reported so far for as-synthesized single-crystalline MoS_2 monolayers.[39,42] The temperature dependence of mobility above ∼100 K is dominated by phonon scattering and can be fitted by a power law $\mu \approx T^{-\gamma}$, where γ describes the dominant phonon scattering mechanism. For our back-gated device, we obtained a value of $\gamma \approx 1.8$, which is slightly larger than theoretical predictions[43] but close to the recent report on monolayer MoS_2 with similar device configuration.[40]

For comparison, we have also tested the electrical performance of the monolayer MoS_2 film grown on a 2 in. h-BN/sapphire wafer. The film together with underlying h-BN was transferred onto a 285-nm-thick SiO_2/Si substrate in order to make back-gated FET device. Figure 5d shows the optical image of the fabricated device array. A two-probe transfer curve of a typical device is shown in Figure 5e, where the extracted mobility is 21.0 $cm^2\ V^{-1}\ s^{-1}$ at room temperature. We measured 60 devices and extracted an average field effect mobility of 23.2 ± 0.2 $cm^2\ V^{-1}\ s^{-1}$ (Figure 5f), which is as expected lower than that of MoS_2 grown on exfoliated h-BN but comparable to the mobility recently reported for a CVD-grown wafer-scale sample.[15]

■ CONCLUSION

In summary, we demonstrate that MBE growth allows precise tuning of the growth parameters (e.g., thickness) and shape control of the nucleated crystals. We carry out growth under the thermodynamically controlled regime that allows the MoS_2 grains to be expitaxially aligned on the h-BN substrate with the same orientation. MoS_2 grains with the same orientation can merge perfectly without forming any grain boundary. As a result, seamless merging of the grains eventually produces a highly crystalline film covering the whole h-BN surface. The availability of high-quality, wafer-scale h-BN enables the large-area heteroepitaxial growth of MoS_2. In view of the wide application of h-BN for passivation and its excellent dielectric property when used in van der Waals heterostructures, our method to grow high-quality crystalline TMDCs on h-BN paves the way for the widespread electronic applications of 2D materials.

■ EXPERIMENTAL SECTION

MoS_2 Growth and Characterization. We used two types of substrates: mechanically exfoliated single-crystalline h-BN flakes on 285-nm-thick SiO_2/Si chips (∼1 cm × 1 cm) and an epitaxially grown

DOI: 10.1021/jacs.7b05131
J. Am. Chem. Soc. 2017, 139, 9392−9400

multilayer h-BN film on a 2 in. sapphire wafer. The film growth was carried out in a customized MBE system with a base pressure of <3 × 10^{-10} Torr. Ultrapure Mo (99.995%, Goodfellow) and S (99.5%, Alfa Aesar) were evaporated from a mini electron-beam evaporator and a valved sulfur cracker cell, respectively. The evaporation of Mo was controlled by setting a constant flux current. The output power was self-adjusted so that the evaporation rate could be kept stable throughout the growth process. The temperature of the sulfur cracker cell was set to 110 °C, and the S evaporation rate was controlled by regulating a motorized valve. The whole growth process was divided into two stages: in the first stage, the substrate was kept at ∼750 °C for 3 to 4 h to form scattered domains; in the second stage, the substrate temperature was increased to ∼900 °C and maintained for an additional 6 to 7 h to allow lateral growth and stitching of the isolated domains to form a monolayer film. The source fluxes were monitored and calibrated by a quartz crystal monitor. The flux ratio between Mo and S at the first stage was kept at about 1:8. At the second stage, the Mo flux was reduced by decreasing the e-beam power while the S flux was kept the same, leading to a flux ratio of about 1:12. The chamber pressure was in the range of 10^{-8}−10^{-7} Torr during growth. After growth, both Mo and S sources were turned off and the sample was annealed in situ at the final growth temperature for 30 min before cooling to room temperature at a rate of 10 °C/min. The as-grown MoS_2 film was checked by AFM (DIMENSION, Veeco Instruments) in tapping mode at room temperature in ambient atmosphere. PL and Raman spectra were taken under a 532 nm laser excitation.

h-BN/Sapphire Sample Preparation. The multilayer h-BN was prepared by a low-pressure CVD method.[38] A *c*-plane sapphire substrate was placed in a CVD system, and ammonia borane (97% purity, Sigma-Aldrich) was placed in a subchamber. The temperature of the furnace was increased to 1400 °C under a flow of Ar gas (10 sccm) and H_2 gas (10 sccm). Ammonia borane was heated to 130 °C in the subchamber. The source was supplied for 30 min, and the pressure was maintained at 0.1 Torr during the growth process. After growth, the furnace was cooled to room temperature under an Ar + H_2 atmosphere.

TEM Sample Preparation and Characterization. The MoS_2/h-BN flakes were transferred onto copper TEM grids by a common polymer-free method where we used 1 M KOH solution as the SiO_2 etchant. STEM imaging was performed on an aberration-corrected Nion UltraSTEM-100 operating at 60 kV. The convergence semiangle for the incident probe was set at 31 mrad. The ADF images were collected for a half angle range of ∼86−200 mrad.

Device Fabrication and Electrical Measurement. For the graphene contacted device, few-layer graphene was exfoliated onto a SiO_2 substrate, followed by a first e-beam lithography patterning to open a rectangular channel. The pre-etched graphene was then wet-transferred onto the as-grown MoS_2 film to form a graphene/MoS_2/h-BN stack. Next, the stack was patterned into a Hall bar structure by a second e-beam lithography and deep reactive ion etching (90% CHF_3, 10% O_2, 40 W). Then, a metal layer of 5 nm Ti and 80 nm Au was deposited on top of the graphene contacted leads of the Hall bar device. After standard metal lift-off, the as-fabricated devices were annealed in forming gas (95% Ar, 5% H_2) at 350 °C for 3 h to remove resist residues and improve the contacts. Finally, an h-BN flake with ∼20 nm thickness was dry-transferred onto the channel area of the device to form the h-BN/MoS2/h-BN sandwich structure (Figure S12). The transport measurements were carried out in an Oxford cryogenic Dewar using a standard lock-in technique (Stanford SR830).

ASSOCIATED CONTENT

Supporting Information

The Supporting Information is available free of charge on the ACS Publications website at DOI: 10.1021/jacs.7b05131.

Additional information (PDF)

AUTHOR INFORMATION

Corresponding Author

*chmlohkp@nus.edu.sg

ORCID

Deyi Fu: 0000-0003-1365-8963
Yu-Yang Zhang: 0000-0002-9548-0021
Hyeon Suk Shin: 0000-0003-0495-7443
Kian Ping Loh: 0000-0002-1491-743X

Author Contributions

○D. Fu and X. Zhao contributed equally to this work.

Notes

The authors declare no competing financial interest.

ACKNOWLEDGMENTS

K.P.L. thanks the National Research Foundation, Prime Minister's Office, for support under the midsized Research Centre (CA2DM). We also acknowledge funding support from the Singapore National Research Foundation (NRF) through the Singapore Berkeley Research Initiative for Sustainable Energy (SinBeRISE) Programme. W.Z. and Y.-Y.Z. acknowledge support from the CAS Pioneer Hundred Talents Program. Work at Vanderbilt University is supported by the U.S. Department of Energy, Grant DE-FG02-09ER46554, and by the McMinn Endowment. The electron microscopy work was supported in part by the U.S. Department of Energy, Office of Science, Basic Energy Science, Materials Sciences and Engineering Division (X.Z. and W.Z.), and through a user project at ORNL's Center for Nanophase Materials Sciences (CNMS), which is a DOE Office of Science User Facility. H.S.S. thanks UNIST and Center for Advanced Soft Electronics for support through the 2016 Research Fund (1.160075) of UNIST and a grant (Code 2011-0031630) from the Center for Advanced Soft Electronics under the Global Frontier Research Program through the National Research Foundation funded by the Ministry of Science, ICT, and Future Planning, Korea.

REFERENCES

(1) Wang, Q. H.; Kalantar-Zadeh, K.; Kis, A.; Coleman, J. N.; Strano, M. S. *Phys. Rev. Lett.* **2010**, *105*, 136805.

(2) Radisavljevic, B.; Radenovic, A.; Brivio, J.; Giacometti, V.; Kis, A. *Nat. Nanotechnol.* **2011**, *6*, 147.

(3) Zeng, H.; Dai, J.; Yao, W.; Xiao, D.; Cui, X. *Nat. Nanotechnol.* **2012**, *7*, 490.

(4) Lopez-Sanchez, O.; Lembke, D.; Kayci, M.; Radenovic, A.; Kis, A. *Nat. Nanotechnol.* **2013**, *8*, 497.

(5) Mak, K. F.; McGill, K. L.; Park, J.; McEuen, P. L. *Science* **2014**, *344*, 1489.

(6) Wu, W.; Wang, L.; Li, Y.; Zhang, F.; Lin, L.; Niu, S.; Chenet, D.; Zhang, X.; Hao, Y.; Heinz, T. F.; Hone, J.; Wang, Z. L. *Nature* **2014**, *514*, 470.

(7) Zhu, H.; Wang, Y.; Xiao, J.; Liu, M.; Xiong, S.; Wong, Z. J.; Ye, Z.; Ye, Y.; Yin, X.; Zhang, X. *Nat. Nanotechnol.* **2015**, *10*, 151.

(8) Sangwan, V. K.; Jariwala, D.; Kim, I. S.; Chen, K.-S.; Marks, T. J.; Lauhon, L. J.; Hersam, M. C. *Nat. Nanotechnol.* **2015**, *10*, 403.

(9) Huang, Y.; Sutter, E.; Shi, N. N.; Zheng, J.; Yang, T.; Englund, D.; Gao, H.-J.; Sutter, P. *ACS Nano* **2015**, *9*, 10612.

(10) Zheng, J.; Zhang, H.; Dong, S.; Liu, Y.; Tai Nai, C.; Suk Shin, H.; Young Jeong, H.; Liu, B.; Ping Loh, K. *Nat. Commun.* **2014**, *5*, 2995.

(11) Lee, Y.-H.; Zhang, X.-Q.; Zhang, W.; Chang, M.-T.; Lin, C.-T.; Chang, K.-D.; Yu, Y.-C.; Wang, J. T.-W.; Chang, C.-S.; Li, L.-J.; Lin, T.-W. *Adv. Mater.* **2012**, *24*, 2320.

DOI: 10.1021/jacs.7b05131
J. Am. Chem. Soc. 2017, 139, 9392−9400

(12) Liu, K.-K.; Zhang, W.; Lee, Y.-H.; Lin, Y.-C.; Chang, M.-T.; Su, C.-Y.; Chang, C.-S.; Li, H.; Shi, Y.; Zhang, H.; Lai, C.-S.; Li, L.-J. *Nano Lett.* **2012**, *12*, 1538.
(13) Chen, W.; Zhao, J.; Zhang, J.; Gu, L.; Yang, Z.; Li, X.; Yu, H.; Zhu, X.; Yang, R.; Shi, D.; Lin, X.; Guo, J.; Bai, X.; Zhang, G. *J. Am. Chem. Soc.* **2015**, *137*, 15632.
(14) Chen, J.; Tang, W.; Tian, B.; Liu, B.; Zhao, X.; Liu, Y.; Ren, T.; Liu, W.; Geng, D.; Jeong, H. Y.; Shin, H. S.; Zhou, W.; Loh, K. P. *Adv. Sci.* **2016**, *3*, 1600033.
(15) Kang, K.; Xie, S.; Huang, L.; Han, Y.; Huang, P. Y.; Mak, K. F.; Kim, C.-J.; Muller, D.; Park, J. *Nature* **2015**, *520*, 656.
(16) van der Zande, A. M.; Huang, P. Y.; Chenet, D. A.; Berkelbach, T. C.; You, Y.; Lee, G.-H.; Heinz, T. F.; Reichman, D. R.; Muller, D. A.; Hone, J. C. *Nat. Mater.* **2013**, *12*, 554.
(17) Najmaei, S.; Liu, Z.; Zhou, W.; Zou, X.; Shi, G.; Lei, S.; Yakobson, B. I.; Idrobo, J.-C.; Ajayan, P. M.; Lou, J. *Nat. Mater.* **2013**, *12*, 754.
(18) Ji, Q.; Zhang, Y.; Gao, T.; Zhang, Y.; Ma, D.; Liu, M.; Chen, Y.; Qiao, X.; Tan, P.-H.; Kan, M.; Feng, J.; Sun, Q.; Liu, Z. *Nano Lett.* **2013**, *13*, 3870.
(19) Dumcenco, D.; Ovchinnikov, D.; Marinov, K.; Lazić, P.; Gibertini, M.; Marzari, N.; Sanchez, O. L.; Kung, Y.-C.; Krasnozhon, D.; Chen, M.-W.; Bertolazzi, S.; Gillet, P.; Fontcuberta i Morral, A.; Radenovic, A.; Kis, A. *ACS Nano* **2015**, *9*, 4611.
(20) Najmaei, S.; Amani, M.; Chin, M. L.; Liu, Z.; Birdwell, A. G.; O'Regan, T. P.; Ajayan, P. M.; Dubey, M.; Lou, J. *ACS Nano* **2014**, *8*, 7930.
(21) Wang, S.; Wang, X.; Warner, J. H. *ACS Nano* **2015**, *9*, 5246.
(22) Yan, A.; Velasco, J.; Kahn, S.; Watanabe, K.; Taniguchi, T.; Wang, F.; Crommie, M. F.; Zettl, A. *Nano Lett.* **2015**, *15*, 6324.
(23) Fu, L.; Sun, Y.; Wu, N.; Mendes, R. G.; Chen, L.; Xu, Z.; Zhang, T.; Rümmeli, M. H.; Rellinghaus, B.; Pohl, D.; Zhuang, L.; Fu, L. *ACS Nano* **2016**, *10*, 2063.
(24) Wan, Y.; Zhang, H.; Wang, W.; Sheng, B.; Zhang, K.; Wang, Y.; Song, Q.; Mao, N.; Li, Y.; Wang, X.; Zhang, J.; Dai, L. *Small* **2016**, *12*, 198.
(25) Wang, W.; Leung, K. K.; Fong, W. K.; Wang, S. F.; Hui, Y. Y.; Lau, S. P.; Chen, Z.; Shi, L. J.; Cao, C. B.; Surya, C. *J. Appl. Phys.* **2012**, *111*, 093520.
(26) Zhang, Y.; Chang, T.-R.; Zhou, B.; Cui, Y.-T.; Yan, H.; Liu, Z.; Schmitt, F.; Lee, J.; Moore, R.; Chen, Y.; Lin, H.; Jeng, H.-T.; Mo, S.-K.; Hussain, Z.; Bansil, A.; Shen, Z.-X. *Nat. Nanotechnol.* **2014**, *9*, 111.
(27) Ugeda, M. M.; Bradley, A. J.; Shi, S.-F.; da Jornada, F. H.; Zhang, Y.; Qiu, D. Y.; Ruan, W.; Mo, S.-K.; Hussain, Z.; Shen, Z.-X.; Wang, F.; Louie, S. G.; Crommie, M. F. *Nat. Mater.* **2014**, *13*, 1091.
(28) Yu, H.; Yang, Z.; Du, L.; Zhang, J.; Shi, J.; Chen, W.; Chen, P.; Liao, M.; Zhao, J.; Meng, J.; Wang, G.; Zhu, J.; Yang, R.; Shi, D.; Gu, L.; Zhang, G. *Small* **2017**, *13*, 1603005.
(29) Splendiani, A.; Sun, L.; Zhang, Y.; Li, T.; Kim, J.; Chim, C.-Y.; Galli, G.; Wang, F. *Nano Lett.* **2010**, *10*, 1271.
(30) Li, H.; Zhang, Q.; Yap, C. C. R.; Tay, B. K.; Edwin, T. H. T.; Olivier, A.; Baillargeat, D. *Adv. Funct. Mater.* **2012**, *22*, 1385.
(31) Shi, H.; Pan, H.; Zhang, Y.-W.; Yakobson, B. I. *Phys. Rev. B: Condens. Matter Mater. Phys.* **2013**, *87*, 155304.
(32) Liu, L.; Feng, Y. P.; Shen, Z. X. *Phys. Rev. B: Condens. Matter Mater. Phys.* **2003**, *68*, 104102.
(33) Zou, X.; Yakobson, B. I. *Small* **2015**, *11*, 4503.
(34) Zhou, W.; Zou, X.; Najmaei, S.; Liu, Z.; Shi, Y.; Kong, J.; Lou, J.; Ajayan, P. M.; Yakobson, B. I.; Idrobo, J.-C. *Nano Lett.* **2013**, *13*, 2615.
(35) Lin, J.; Cretu, O.; Zhou, W.; Suenaga, K.; Prasai, D.; Bolotin, K. I.; Cuong, N. T.; Otani, M.; Okada, S.; Lupini, A. R.; Idrobo, J.-C.; Caudel, D.; Burger, A.; Ghimire, N. J.; Yan, J.; Mandrus, D. G.; Pennycook, S. J.; Pantelides, S. T. *Nat. Nanotechnol.* **2014**, *9*, 436.
(36) Hÿtch, M. J.; Snoeck, E.; Kilaas, R. *Ultramicroscopy* **1998**, *74*, 131.
(37) Jang, A. R.; Hong, S.; Hyun, C.; Yoon, S. I.; Kim, G.; Jeong, H. Y.; Shin, T. J.; Park, S. O.; Wong, K.; Kwak, S. K.; Park, N.; Yu, K.; Choi, E.; Mishchenko, A.; Withers, F.; Novoselov, K. S.; Lim, H.; Shin, H. S. *Nano Lett.* **2016**, *16*, 3360.
(38) Kim, S. M.; Hsu, A.; Park, M. H.; Chae, S. H.; Yun, S. J.; Lee, J. S.; Cho, D.-H.; Fang, W.; Lee, C.; Palacios, T.; Dresselhaus, M.; Kim, K. K.; Lee, Y. H.; Kong, J. *Nat. Commun.* **2015**, *6*, 8662.
(39) Radisavljevic, B.; Kis, A. *Nat. Mater.* **2013**, *12*, 815.
(40) Cui, X.; Lee, G.-H.; Kim, Y. D.; Arefe, G.; Huang, P. Y.; Lee, C.-H.; Chenet, D. A.; Zhang, X.; Wang, L.; Ye, F.; Pizzocchero, F.; Jessen, B. S.; Watanabe, K.; Taniguchi, T.; Muller, D. A.; Low, T.; Kim, P.; Hone, J. *Nat. Nanotechnol.* **2015**, *10*, 534.
(41) Wang, L.; Meric, I.; Huang, P. Y.; Gao, Q.; Gao, Y.; Tran, H.; Taniguchi, T.; Watanabe, K.; Campos, L. M.; Muller, D. A.; Guo, J.; Kim, P.; Hone, J.; Shepard, K. L.; Dean, C. R. *Science* **2013**, *342*, 614.
(42) Baugher, B. W. H.; Churchill, H. O. H.; Yang, Y.; Jarillo-Herrero, P. *Nano Lett.* **2013**, *13*, 4212.
(43) Kaasbjerg, K.; Thygesen, K. S.; Jacobsen, K. W. *Phys. Rev. B: Condens. Matter Mater. Phys.* **2012**, *85*, 115317.

DOI: 10.1021/jacs.7b05131
J. Am. Chem. Soc. 2017, 139, 9392−9400